Label-free classification of hepatocellular-carcinoma grading using second harmonic generation microscopy

HONGXIN LIN,[1,3] LIYAN LIN,[2,3] GUANGXING WANG,[1] NING ZUO,[1] ZHENLIN ZHAN,[1] SHUSEN XIE,[1] GANG CHEN,[2] JIANXIN CHEN,[1] AND SHUANGMU ZHUO[1,*]

[1]*Key Laboratory of OptoElectronic Science and Technology for Medicine of Ministry of Education & Fujian Provincial Key Laboratory of Photonics Technology, Fujian Normal University, Fuzhou 350007, China*
[2]*Department of Pathology, Fujian Cancer Hospital & Fujian Medical University Cancer Hospital, Fuzhou 350014, China*
[3]*These authors contributed equally to this work.*
*shuangmuzhuo@gmail.com

Abstract: The clear and accurate understanding of the degree of hepatocellular-carcinoma (HCC) differentiation plays a key role in the determination of the patient prognosis and development of a treatment plan by the clinician. However, label-free and automated classification of the HCC grading is challenging. Here, we demonstrate second-harmonic generation (SHG) microscopy for label-free classification of HCC grading in paraffin-embedded specimens. A total of 217 images from 113 patients were obtained using SHG microscopy, and the SHG signals from the collagen within the tumor were analyzed using feature extraction and selection, the Mann–Whitney test, and the receiver operating characteristic curves. The results exhibit good correlation between the software analysis and the diagnosis by experienced pathologists. Combining the image features and clinical information, an adaptive quantification algorithm is generated for automatically determining the HCC grade. The results suggest that SHG microscopy might be a promising automated diagnostic method for clinical use, without requiring time for tissue processing and staining.

References and links

1. X. W. Wang, J. W. Grisham, and S. S. Thorgeirsson, *Molecular Genetics of Liver Neoplasia* (Springer, 2011) Chap. 1.
2. W. Chen, R. Zheng, P. D. Baade, S. Zhang, H. Zeng, F. Bray, A. Jemal, X. Q. Yu, and J. He, "Cancer statistics in China, 2015," CA Cancer J. Clin. **66**(2), 115–132 (2016).
3. T. Liu, C. Hsieh, Y. Chen, F. Huang, H. Huang, W.-J. Lee, C.-T. Kung, and C.-K. Sun, "Diagnosing hepatocellular carcinoma with the intensity and the lifetime of two-photon red autofluorescences," Proc. SPIE **7903**, 79032Z (2011).
4. P. Bedossa, "Intraobserver and interobserver variations in liver biopsy interpretation in patients with chronic hepatitis C," Hepatology **20**(1 Pt 1), 15–20 (1994).
5. K. Grønbaek, P. B. Christensen, S. Hamilton-Dutoit, B. H. Federspiel, E. Hage, O. J. Jensen, and M. Vyberg, "Interobserver variation in interpretation of serial liver biopsies from patients with chronic hepatitis C," J. Viral Hepat. **9**(6), 443–449 (2002).
6. I. Freund, M. Deutsch, and A. Sprecher, "Connective tissue polarity. Optical second-harmonic microscopy, crossed-beam summation, and small-angle scattering in rat-tail tendon," Biophys. J. **50**(4), 693–712 (1986).
7. I. Freund and M. Deutsch, "Macroscopic polarity of connective tissue is due to discrete polar structures," Biopolymers **25**(4), 601–606 (1986).
8. I. Freund and M. Deutsch, "Second-harmonic microscopy of biological tissue," Opt. Lett. **11**(2), 94 (1986).
9. T. Y. Sun, A. M. Haberman, and V. Greco, "Preclinical advances with multiphoton microscopy in live imaging of skin cancers," J. Invest. Dermatol. **137**(2), 282–287 (2017).

10. M. Han, L. Zickler, G. Giese, M. Walter, F. H. Loesel, and J. F. Bille, "Second-harmonic imaging of cornea after intrastromal femtosecond laser ablation," J. Biomed. Opt. **9**(4), 760–766 (2004).
11. C. A. Thorling, D. Crawford, F. J. Burczynski, X. Liu, I. Liau, and M. S. Roberts, "Multiphoton microscopy in defining liver function," J. Biomed. Opt. **19**(9), 090901 (2014).
12. M. Strupler, A. M. Pena, M. Hernest, P. L. Tharaux, J. L. Martin, E. Beaurepaire, and M. C. Schanne-Klein, "Second harmonic imaging and scoring of collagen in fibrotic tissues," Opt. Express **15**(7), 4054–4065 (2007).
13. J. Xu, Y. Chen, H. Chen, Z. Hong, Z. Shi, S. Zhuo, X. Zhu, and J. Chen, "Identifying the neck margin status of ductal adenocarcinoma in the pancreatic head by multiphoton microscopy," Sci. Rep. **7**(1), 4586 (2017).
14. J. Xu, D. Kang, Y. Zeng, S. Zhuo, X. Zhu, L. Jiang, J. Chen, and J. Lin, "Multiphoton microscopy for label-free identification of intramural metastasis in human esophageal squamous cell carcinoma," Biomed. Opt. Express **8**(7), 3360–3368 (2017).
15. J. Yan, S. Zhuo, G. Chen, X. Wu, D. Zhou, S. Xie, J. Jiang, M. Ying, F. Jia, J. Chen, and J. Zhou, "Preclinical study of using multiphoton microscopy to diagnose liver cancer and differentiate benign and malignant liver lesions," J. Biomed. Opt. **17**(2), 026004 (2012).
16. S. Xu, D. Tai, A. Wee, R. Welsch, P. So, H. Yu, J. Rajapakse, "Automated scoring of liver fibrosis through combined features from different collagen groups," IEEE EMBS, **2011**, 4503–4506 (2011).
17. P. J. Campagnola and L. M. Loew, "Second-harmonic imaging microscopy for visualizing biomolecular arrays in cells, tissues and organisms," Nat. Biotechnol. **21**(11), 1356–1360 (2003).
18. S. Zhuo and M. Ni, "Label-free and real-time imaging of dehydration-induced DNA conformational changes in cellular nucleus using second harmonic microscopy," Sci. Rep. **4**(1), 7416 (2014).
19. S. Zhuo, J. Chen, T. Luo, D. Zou, and J. Zhao, "Multimode nonlinear optical imaging of the dermis in ex vivo human skin based on the combination of multichannel mode and Lambda mode," Opt. Express **14**(17), 7810–7820 (2006).
20. J. Li, Z. Zhan, J. Chen, and S. Zhuo, "Quantitative optical biomarkers of lung cancer based intrinsic two-photon excited fluorescence signal," Proc. SPIE **24**, 100242I (2016).
21. S. M. Zhuo, J. X. Chen, G. Z. Wu, S. S. Xie, L. Q. Zheng, X. S. Jiang, and X. Q. Zhu, "Quantitatively linking collagen alteration and epithelial tumor progression by second harmonic generation microscopy," Appl. Phys. Lett. **96**(21), 213704 (2010).
22. A. Zoumi, A. Yeh, and B. J. Tromberg, "Imaging cells and extracellular matrix in vivo by using second-harmonic and two-excited fluorescence," Proc. Natl. Acad. Sci. U.S.A. **99**, 11014–11019 (2002).
23. A. P. Dempster, N. M. Laird, and D. B. Rubin, "Maximum likelihood from incomplete data via the EM algorithm," J. R. Stat. Soc. [Ser A] **39**(1), 1–38 (1977).
24. A. M. Stein, D. A. Vader, L. M. Jawerth, D. A. Weitz, and L. M. Sander, "An algorithm for extracting the network geometry of three-dimensional collagen gels," J. Microsc. **232**(3), 463–475 (2008).
25. A. Theodossi, A. M. Skene, B. Portmann, R. P. Knill-Jones, R. S. Patrick, R. A. Tate, W. Kealey, K. J. Jarvis, D. J. O'Brian, and R. Williams, "Observer variation in assessment of liver biopsies including analysis by kappa statistics," Gastroenterology **79**(2), 232–241 (1980).
26. A. Theodossi, D. J. Spiegelhalter, J. Jass, J. Firth, M. Dixon, M. Leader, D. A. Levison, R. Lindley, I. Filipe, and A. Price, "Observer variation and discriminatory value of biopsy features in inflammatory bowel disease," Gut **35**(7), 961–968 (1994).
27. J. Westin, L. M. Lagging, R. Wejstål, G. Norkrans, and A. P. Dhillon, "Interobserver study of liver histopathology using the Ishak score in patients with chronic hepatitis C virus infection," Liver **19**(3), 183–187 (1999).
28. S. Tamura, T. Kato, M. Berho, E. P. Misiakos, C. O'Brien, K. R. Reddy, J. R. Nery, G. W. Burke, E. R. Schiff, J. Miller, and A. G. Tzakis, "Impact of histological grade of hepatocellular carcinoma on the outcome of liver transplantation," Arch. Surg. **136**(1), 25–30, discussion 31 (2001).
29. T. M. Pawlik, K. A. Delman, J. N. Vauthey, D. M. Nagorney, I. O. Ng, I. Ikai, Y. Yamaoka, J. Belghiti, G. Y. Lauwers, R. T. Poon, and E. K. Abdalla, "Tumor size predicts vascular invasion and histologic grade: Implications for selection of surgical treatment for hepatocellular carcinoma," Liver Transpl. **11**(9), 1086–1092 (2005).
30. L. Gailhouste, Y. Le Grand, C. Odin, D. Guyader, B. Turlin, F. Ezan, Y. Désille, T. Guilbert, A. Bessard, C. Frémin, N. Theret, and G. Baffet, "Fibrillar collagen scoring by second harmonic microscopy: a new tool in the assessment of liver fibrosis," J. Hepatol. **52**(3), 398–406 (2010).
31. S. Xu, Y. Wang, D. C. S. Tai, S. Wang, C. L. Cheng, Q. Peng, J. Yan, Y. Chen, J. Sun, X. Liang, Y. Zhu, J. C. Rajapakse, R. E. Welsch, P. T. C. So, A. Wee, J. Hou, and H. Yu, "qFibrosis: a fully-quantitative innovative method incorporating histological features to facilitate accurate fibrosis scoring in animal model and chronic hepatitis B patients," J. Hepatol. **61**(2), 260–269 (2014).

1. Introduction

Liver cancer is the fifth most common cancer worldwide, and is the third deadliest [1]. According to the cancer statistics of China, in 2015, 466100 new cases and 422100 deaths were estimated, ranking third and fourth as the cause of male and female mortality, respectively [2]. Hepatocellular carcinoma (HCC) comprises more than 90% of liver cancer.

HCC patients with the different grades of tumor can have drastically different treatment responses and overall outcomes; therefore, the clear and accurate understanding of the degree of HCC differentiation is of immense clinical value.

Currently, the HCC grade is difficult to classify, and relies only on the expertise of the concerned pathologist and the time taken for diagnosis [3]. Figure 1 shows typical images of haematoxylin and eosin (H&E)-stained HCC of different grades, and a sample of the normal liver tissue for comparison. Traditional grading systems, originally formulated for liver disease, focus more on the qualitative rather than quantitative characteristics of cancer development. Owing to intra- and inter-observer variations, it is difficult to obtain highly reproducible results, reliably and sufficiently [4, 5]. Moreover, capturing and assessing collagen-related diagnostic information is impossible by using H&E staining. Therefore, the development of a new method for the label-free, and automated classification of the HCC grading is medically significant.

In 1986, Freund et al. reported the second-harmonic-generation (SHG) data of a rat-tail tendon for the first time [6–8]. Subsequently, SHG microscopy was not only widely applied for collagen imaging the skin [9], cornea [10], liver [11], and kidney [12], but also used for determining whether the tumor was benign or malignant and likely to recur. Collagen, which has special and orderly structural properties, can be exhibited clearly. The tumor is identified by observing the SHG images and analyzing the content, direction angle, and length of the collagen fiber [13, 14]. In particular, our previous study has proved that it is feasible to differentiate benign and malignant liver cancer via SHG microscopy [15]. As efforts for exploiting SHG microscopy for the label-free, and automated classification of HCC grading have not been reported thus far, we undertook this study, using the technique.
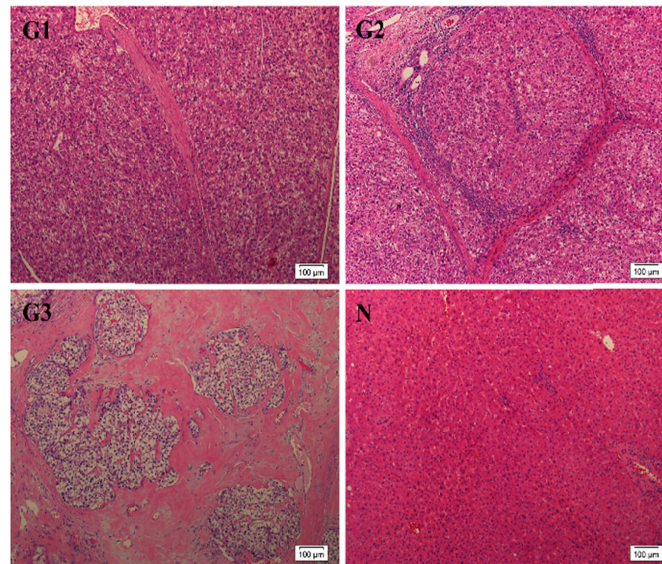

Fig. 1. Various differentiation states of hepatocellular carcinoma. G1, G2, and G3 are the grading states, during tumor genesis, and N represents a H&E stained sample of a healthy liver tissue with normal cells. Scale bar = 100 μm.

2. Materials and methods

2.1 Workflow

A workflow integrating SHG microscopy, histopathology, and software was established (Fig. 2). Initially, the thin sections of the tumor were measured by SHG microscopy, using a commercial laser scanning microscopic imaging system (Zeiss LSM 880, Jena, Germany).

The obtained images were then clustered by a supervised algorithm, in the training stage. The resulting SHG image represented the collagen distribution, over the examined tissue section. Meanwhile, the tumor section was still accessible for H&E staining. In collaboration with pathologists, the collagen distribution, based on the SHG image, was correlated with the classically stained image of the sample. A collagen database was generated for different grading types, based on expert annotation, enabling us to build an adaptive quantification algorithm.
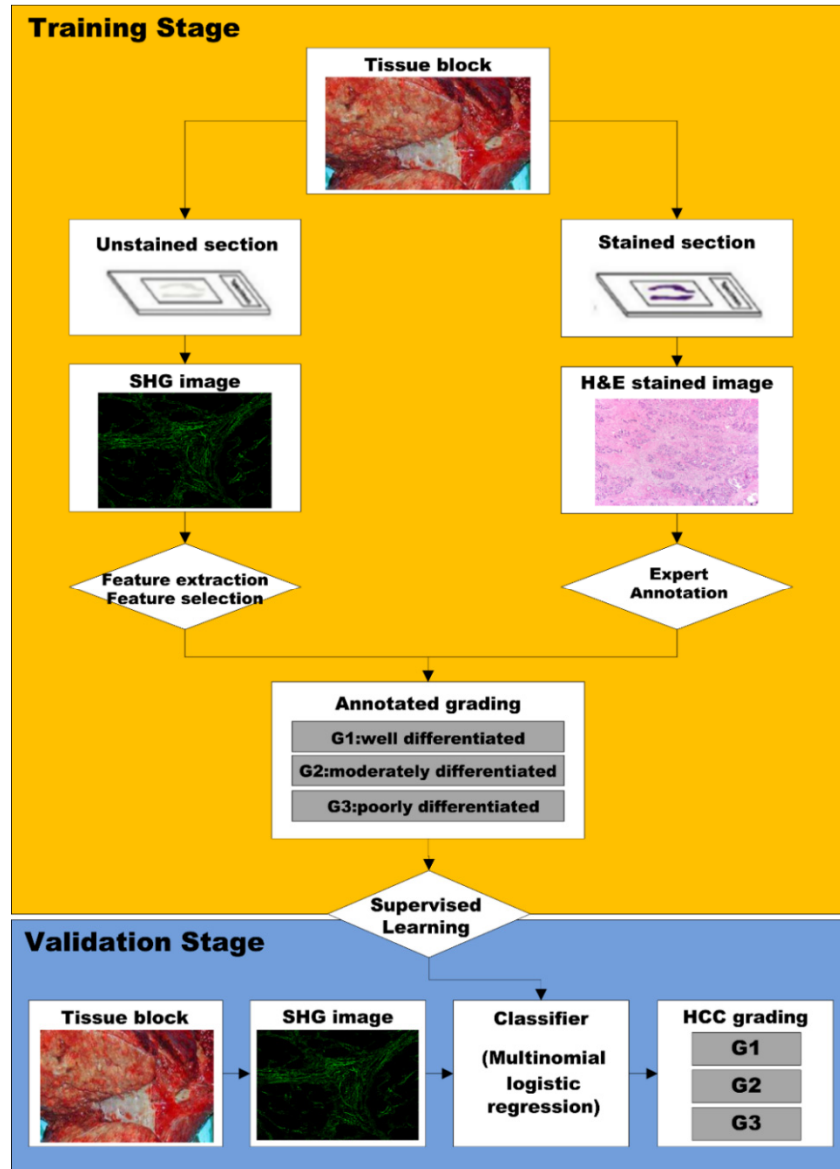

Fig. 2. Workflow of the training and validation stage. In the training stage, the SHG images were correlated with classical histopathological annotation, by an expert. The resulting database was used for the adaptive quantification algorithm, which was validated on independent samples in the validation stage.

The procedure for building the adaptive quantification algorithm included the identification of different collagen patterns (the aggregated or the distributed), the extraction

of collagen morphological features (percentage, length, width, cross-link density and space, etc.), the statistical analysis of features of the respective collagen, which were then drawn into the boxplots, and establishment of multinomial logistic regression model [16]. The used algorithm was implemented in the MATLAB 2015b programming environment.

2.2 Tissue-sample preparation

To obtain a large sample size and relevant clinical data, formalin-fixed, paraffin-embedded (FFPE) tissues were used in this study. All the archival FFPE tissues were diagnosed at the Fujian provincial tumor hospital. The tissue samples were cut into two 5~10 μm-thick pieces for SHG imaging and H&E staining, respectively. A trained pathologist independently read and staged the stained samples, using the WHO grading system. This work included 113 patients, who underwent surgical biopsies from 2011 to 2017 (Table 1), and it was approved by the institutional review board of the Fujian provincial tumor hospital.

Table 1. Summary of the experimental samples with different gradings

Gradings	Total	Sex	age	Tumor embolus	Relapse	Metastasis
G1	34 (70)	Male 26 Female 8	>50 13 ≤50 21	23	19	8
G2	39 (68)	Male 31 Female 8	>50 12 ≤50 17	16	16	1
G3	40 (79)	Male 36 Female 4	>50 32 ≤50 8	9	10	2

2.3 Image acquisition

Because the formalin and paraffin are not effective in generating SHG signal and the collagen is only capable of emitting strong SHG signal [17], the SHG imaging contrast in the FFPE tissues is not to be altered. In this work, we only used SHG microscopy for the classification of HCC grading. Specifically, SHG images of the unstained sections of the tissue samples were acquired using the Zeiss LSM 880 coupled with a femtosecond Ti: sapphire laser operating at 810 nm [18, 19]. An objective was employed to focus the excitation beam into the sample and collect the backscattered SHG signals. To obtain a big field of view (850 × 850 μm^2), a 10 × objective was chosen in this work. A fine focusing stage was used to translate the samples after x-y scan of the samples for obtaining a large-area image (8 × 8 mm^2). This system has several channels and each channel can be set selectively for accepting emission signals within a random range of 370–700 nm, to obtain the images. In this study, one of the channels (370–419 nm, green color-coded) was used for collecting the SHG signals [20]. Selection of the excitation wavelength is optimal for SHG imaging [21, 22].

2.4 Histopathological scoring

Currently, tumor histopathologic classification relies on the WHO grading system, based on the degree of staining of the acidophilia in the cancer cell cytoplasm, the size of the nuclei, nucleoplasm ratio, depth of the nuclear staining, cell functions, and tissue structures. Tumors are graded as well-differentiated (G1), moderately differentiated (G2), poorly differentiated (G3), and undifferentiated (G4). In G1, the tumor cells and tissue structures, which are referred to as low grade, are similar to the normal ones. In contrast, the cells and tissue of G3 and G4 grow rapidly and spread faster, and are referred to as high grade [https://www.cancer.gov/about-cancer/diagnosis-staging/prognosis/tumor-grade-fact-sheet].
In this study, the 217 HCC samples included 79 poorly differentiated, 68 moderately differentiated, and 70 well-differentiated ones.

2.5 Statistical analysis

The two-tailed Mann–Whitney test was used for assessing the statistical differences between the HCC gradings. The receiver operating characteristic (ROC) curves and the area under the

ROC (AUC) were obtained to detect the various HCC gradings, using SPSS 22.0. A specific multinomial logistic regression model was built using MATLAB 2015b for combining the best image and clinical features to obtain a higher recognition rate. Then, $p<0.05$ was defined as statistically significant.

3. Results

3.1 SHG-revealed HCC collagen architectures

A prospective study, with 217 surgical specimens from 113 patients, was performed to evaluate the diagnostic accuracy of SHG, compared to that by a pathologist. Figure 3 displays three 8×8-mm^2 SHG images of G1, G2, and G3, respectively. The entire SHG distribution within the tumor was mainly revealed by low enlargement ($10 \times$), and the collagen localization was displayed clearly and precisely. As observed in Fig. 3(A), the collagen in G1 is negligible and scattered in a slender strip, similar to a normal liver. Within the tumor in G2 (Fig. 3(B)), an obvious increase was observed in the collagen; each piece of collagen had grown longer and thicker, from the initial shape. The collagen was spread in the shape of spider webs, within a typical tumor, in G3 (Fig. 3(C)).
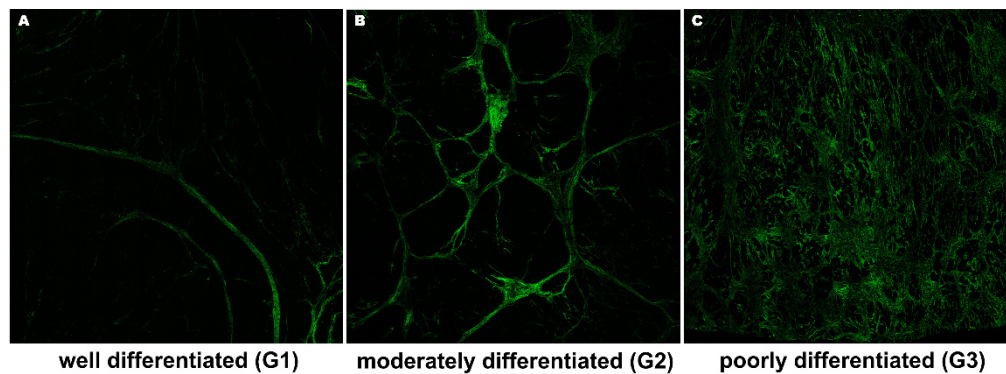

well differentiated (G1)   moderately differentiated (G2)   poorly differentiated (G3)

Fig. 3. Representative SHG images of HCC in G1, G2, and G3. The size of images is 8×8 mm^2.

3.2 HCC quantitative assessment

The image processing consists of two main steps. First, the acquired SHG images were segmented into collagen and background by a segmentation algorithm based on Gaussian mixture models [23]. Second, the identification of aggregated and distributed collagen, and the further extraction of collagen morphological features were performed using a fiber network extraction algorithm [24] based on the binary image of the segmented collagen. In this process, the number of cross-links per fiber determined the collagen pattern, and the data sets of the image features were obtained. A set of data included 13 collagen architectural features, such as the aggregated collagen percentage, distributed collagen percentage, total collagen percentage, fiber number, fiber length, fiber width, cross-link density, cross-link space, ratio between the aggregated and total collagen, etc.

217 HCC images were processed, including 70 images from G1, 68 images from G2, and 79 images from G3. Through the two-tailed Mann–Whitney test of each parameter between different HCC grading, we drew the following conclusion and presented them in the boxplots. Six parameters exhibited significant differences and an obvious increase, when the grading changed from G1–G3 ($p<0.05$) (Fig. 4). The other seven parameters exhibited no discernible differentiation between the two-tailed contrasts. Four characteristics, namely, the cross-link density, space of the aggregated collagen, and the distributed collagen length and width, could be distinguished between G2 and G3, but not between G1 and G2. The three characteristic parameters, namely, the aggregated collagen length and width, and the ratio between the

aggregated and total collagen, were statistically significant in G1 and G2. However, there were no statistical differences between G2 and G3 (Fig. 5).
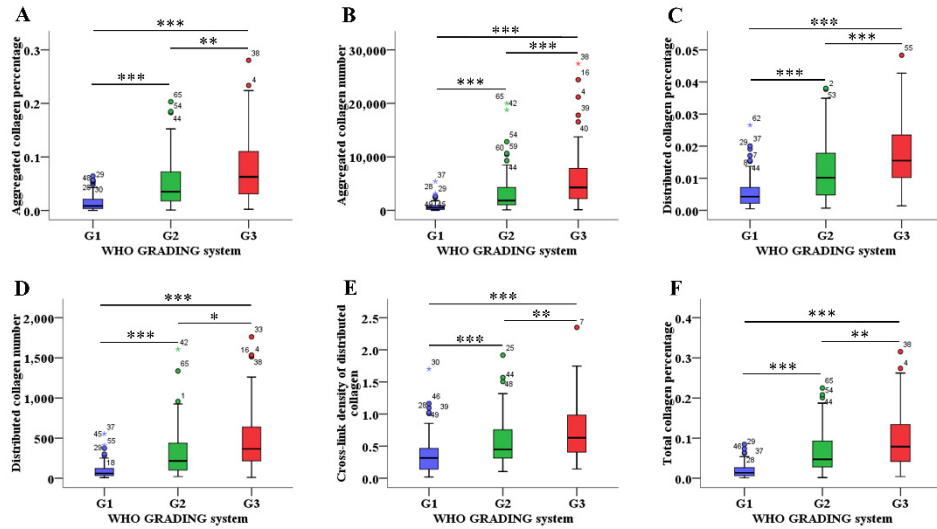

Fig. 4. Changes in six features, between the various HCC gradings: (A) aggregated collagen percentage, (B) number, (C) distributed collagen percentage, (D) number, (E) cross-link density, and (F) total collagen percentage. The boxes indicate the median 25th and 75th percentiles, whereas the bars display the adjacent values. The "*" symbol represents $p<0.05$, "**" represents $p<0.01$, and "***" represents $p<0.001$.
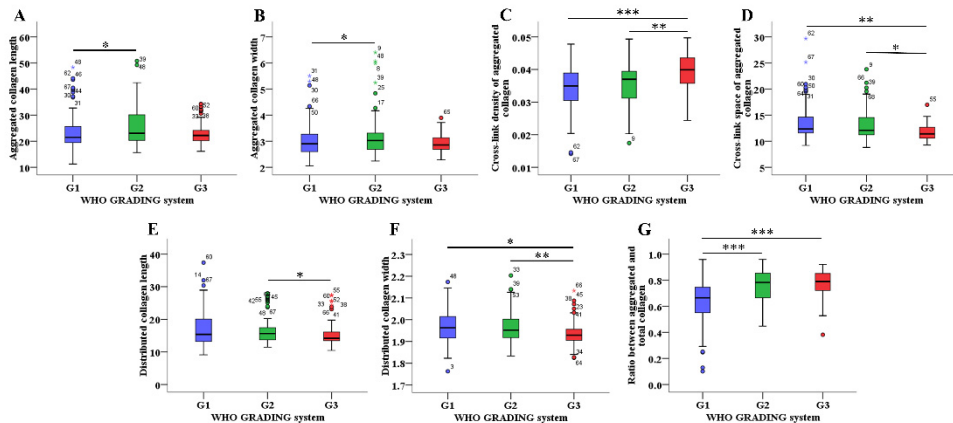

Fig. 5. Changes in seven features, between the various HCC gradings: (A) aggregated collagen length, (B) width, (C) cross-link density, (D) cross-link space, (E) distributed collagen length, (F) width and, (G) ratio between the aggregated and total collagen The boxes indicate the median 25th and 75th percentiles, whereas the bars display the adjacent values. The "*" symbol represents $p<0.05$, "**" represents $p<0.01$, and "***" represents $p<0.001$.

3.3 Detection of G1 and G3

We further analyzed the correlation between the collagen architectural features and the WHO grading system, which is the widely applied standard for HCC classification. Tables 2 and 3 recorded the AUC value, the cut-off value, sensitivity, and specificity of each feature in two groups G1 *vs*. G2G3 and G1G2 *vs*. G3. Based on the ROC-curve analysis (Fig. 6 and Fig. 7),

we determined that five parameters could effectively identify the well-differentiated (G1) from the moderately and poorly differentiated (G2 and G3). The AUC of the aggregated collagen number was the largest with a value was 0.890 (Fig. 7(A)). The cut-off value was 0.70, between the sensitivity (84.1%) and specificity (85.7%). The AUC values of four other parameters, the aggregated collagen percentage, distributed collagen number, distributed collagen percentage, and total collagen percentage, were lesser (0.822-0.870) (Fig. 7(A), Table 2). Effectively distinguishing the poorly-differentiated (G3) from the well- and moderately differentiated (G1 and G2), as shown in Fig. 7(B), the AUC values of the aggregated collagen number and distributed collagen number were 0.821 and 0.807, respectively. For the aggregated collagen number, the cut-off value was 0.54, between the sensitivity (87.1%) and specificity (66.9%). The cut-off values (0.51), corresponding to the sensitivity (84.3%) and specificity (66.2%) were determined, for the distributed collagen number (Table 3).
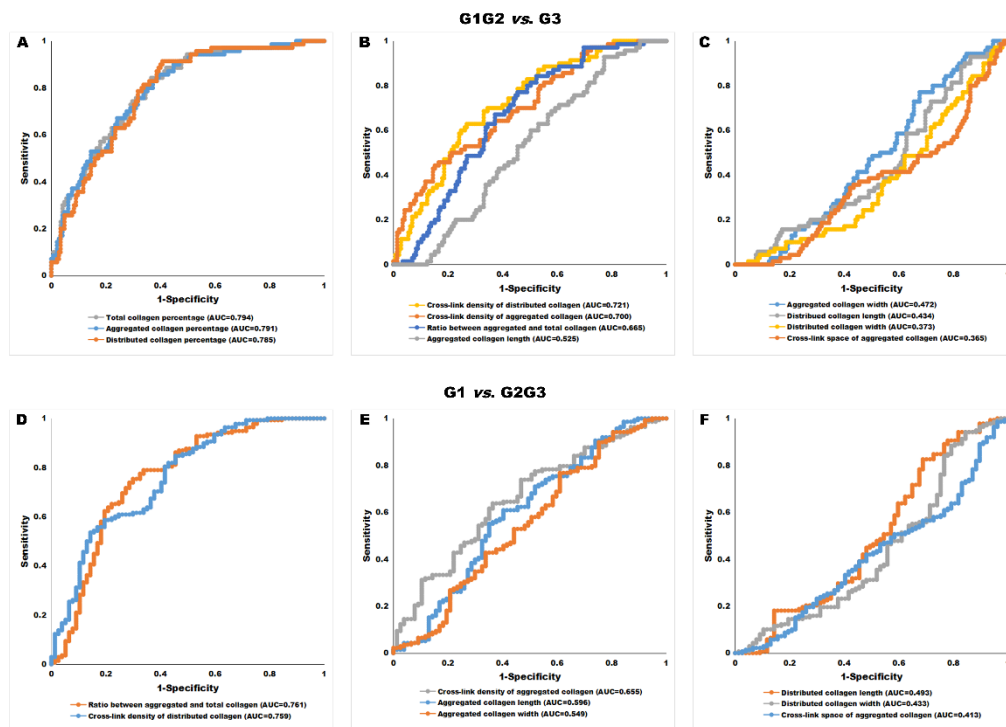

Fig. 6. (A) ROC analysis of three parameters: the collagen percentage including the total, the aggregated and the distributed, to identify G3 from G1 and G2; (B) ROC analysis of four parameters: the cross-link density of aggregated and distributed collagen, the ratio between aggregated and total collagen, and the aggregated collagen length, to identify G3 from G1 and G2; (C) ROC analysis of four parameters: the aggregated collagen width, the distributed collagen length and width, and cross-link space of aggregated collagen, to identify G3 from G1 and G2; (D) ROC analysis of two parameters: the ratio between aggregated and total collagen, and the cross-link density of distributed collagen, to detect G1 from G2 and G3; (E) ROC analysis of three parameters: the cross-link density of aggregated collagen, and the aggregated collagen length and width, to detect G1 from G2 and G3; (F) ROC analysis of three parameters: the distributed collagen length and width, and the cross-link space of aggregated collagen, to detect G1 from G2 and G3.
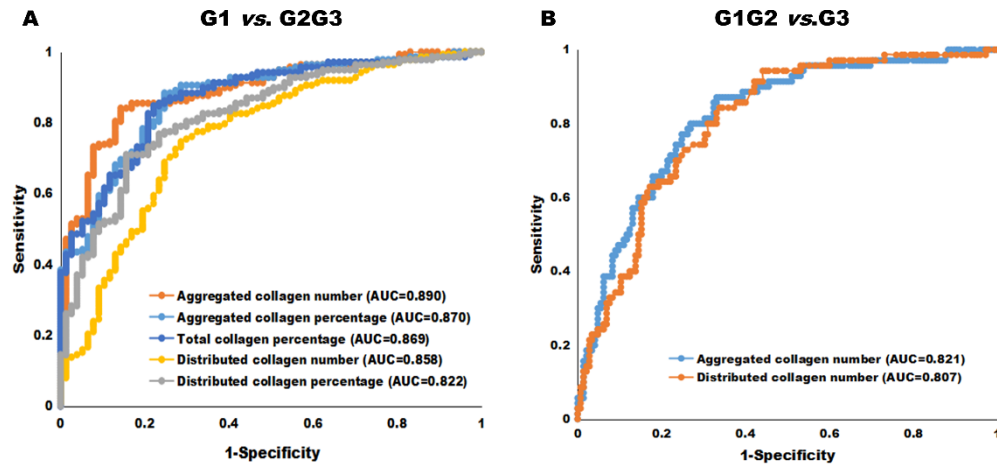
Fig. 7. (A) ROC analysis of five parameters: the aggregated collagen number and percentage, total collagen percentage, and the distributed collagen number and percentage, to identify G1 from G2 and G3, and (B) ROC analysis of two parameters: the aggregated collagen number and distributed collagen number, to detect G3 from G1 and G2.

Table 2. The AUC value, cut-off value, sensitivity, and specificity of the SHG image features, for detecting G1.

G1 vs. G2G3	Aggregated collagen						Distributed collagen					Total collagen percentage	Ratio between aggregated and total collagen
	Percentage	Number	Length	Width	Cross-link density	Cross-link space	Percentage	Number	Length	Width	Cross-link density		
AUC value	0.87	0.89	0.596	0.549	0.655	0.413	0.822	0.858	0.493	0.433	0.759	0.869	0.761
Cut-off value	0.64	0.70	0.21	0.16	0.27	0.18	0.55	0.59	0.14	0.21	0.39	0.63	0.46
Sensitivity (%)	88.4	84.1	60.9	76.8	63.8	63.8	71	76.1	82.6	31.2	53.6	84.8	75.4
Specificity (%)	75.3	85.7	59.7	39	63.6	18.2	84.4	83.1	31.2	48.1	85.7	77.9	70.1

Table 3. The AUC value, cut-off value, sensitivity, and specificity of the SHG image features, for detecting G3.

G1G2 vs. G3	Aggregated collagen						Distributed collagen					Total collagen percentage	Ratio between aggregated and total collagen
	Percentage	Number	Length	Width	Cross-link density	Cross-link space	Percentage	Number	Length	Width	Cross-link density		
AUC value	0.791	0.821	0.525	0.472	0.7	0.365	0.785	0.807	0.434	0.373	0.721	0.794	0.665
Cut-off value	0.46	0.54	0.16	0.14	0.29	0.25	0.51	0.51	0.19	0.27	0.36	0.48	0.32
Sensitivity (%)	85.7	87.1	92.9	2.9	45.7/44.3	54.3	91.4	84.3	30	17.1	62.9	84.3	84.3
Specificity (%)	60.7	66.9	22.8	83.4	83.4/84.8	20.7	59.3	66.2	51	55.9	73.1	63.4	47.6

3.4 Adaptive quantification algorithm

Combining 13 image features with seven clinical information, we used the logistic regression algorithm to automatically score 20 characteristics (0-1). Irrespective of whether the feature was clinical or an image, the characteristics were selected, if their scores were greater than 0.5. The selected features were analyzed by a specific multinomial logistic regression model for building the adaptive quantification algorithm. 80% of the entire data was set as the training data and 20% as the validation data. The recognition accuracy reached 91%.

4. Discussion

By well correlating the spatial architectural features of SHG images and the pathologist diagnosis, we generated an adaptive quantification algorithm that can reliably classify the HCC grading. This algorithm can minimize the influence of sampling error and the intra/inter observer discrepancies [25–27].

As the SHG imaging method has several advantages, it is a perfect substitute for conventional histological imaging. The samples are not deteriorated or photo-damaged. Regardless of the sample-preparation type, SHG microscopy can image not only the frozen-section but also the paraffin-embedded tissues. Moreover, a 3D reconstruction of the fibrillar collagen is achieved, in each case. Although postoperative paraffin-embedded H&E histology is considered as the gold standard of HCC grading diagnosis, approximately 16 h is required for fixation, processing, and staining. Intraoperative frozen-section analysis with SHG microscopy can significantly reduce the diagnosis time, and obtain quick and effective feedback by eliminating the time consumed for tissue processing and staining.

This study is based on traditional histopathologic grading. In order to monitor the growth of the tumor, we imaged the spatial architectural features of the fibrillar collagen within the tumor. The majority of HCC growth progress from a regenerative nodule to atypical hyperplasia, further progressing to well-differentiated HCC, and finally to moderately or poorly differentiated HCC. When the tumor diameter reaches 2 cm, the poorly differentiated region replaces the well-differentiated one, with the malignant biological characteristics of HCC. This behavior proves that the degree of grading plays a significant role in the prognosis of HCC [28]. In addition, HCC histologic grade extremely impacts the outcome of surgical treatments [29]. Thus, it is an important factor that influences the intraoperative decision-making, postoperative recurrence rate, survival rate, and life-quality of patients. As the HCC differentiation reduces, its invasiveness gradually increases, and the survival prognosis of the patient worsens. Hence, the clear and accurate understanding of the degree of HCC differentiation is beneficial for clinicians, for determining a comprehensive treatment in the perioperative period.

With the same SHG imaging method, Gailhouste et al. first combined the SHG signal and the collagen forms to develop the fibrosis-SHG index. This innovative method was routinely applied to biopsies from 119 patients with chronic liver disease for measuring the fibrosis area, during fibrosis progression [30]. Xu et al. combined 87 parameters of the collagen architectural features from 25 rat samples and 162 chronic hepatitis-B patients to establish the qFibrosis, which can identify all the METAVIR stages reliably and faithfully [31]. Our study provides a highly reproducible quantification algorithm, which can be used as a standard platform for assessing HCC progression. For the same samples, different pathologists may arrive at inconsistent diagnostic conclusions; whereas, in other cases, different regions of the same sample may be diagnosed with different types of differentiation. Our method can solve the above-mentioned discrepancies. The tumor-cell differentiation and an incomplete envelope are significant markers of the malignant transformation of the tumor biological characteristics. Furthermore, considering the architectural features of the tumor-enveloped fibers and the peripheral fibers of blood vessels, we intend to expand the imaging range and upgrade the quantification algorithm, as the next step.

Currently, it is impossible to obtain or ignore HCC differentiation, in general, because ablation therapy is increasingly applied to early HCC. However, according to reports, it is easier to transfer poorly-differentiated HCC by needle after radiofrequency ablation, which has greater risk of intrahepatic metastasis. Therefore, it is important to predict the degree of differentiation of early HCC before surgery. Some studies suggest that clinicians can resort to liver resection instead of radiofrequency ablation for early poorly differentiated HCC, for better prognosis. On the other hand, before liver transplantation, patients and clinicians should consider the biological characteristics of the tumor, particularly, the histological differentiation. Poorly differentiated HCC leads to shorter survival time and higher recurrence rates. In addition, it serves as the theoretical basis for the rational use of organs, in case of organ shortage.

5. Conclusion

In summary, we combined SHG microscopy, histopathology, and software to rapidly classify HCC grading, which provides more accurate information for tumor detection and therapy. It was demonstrated that SHG images cannot only distinguish HCC differentiation by the Mann-Whitney test, boxplot, and ROC analysis, but can also be used for generating an adaptive quantification algorithm to calculate the recognition rate. As a visual method, SHG microscopy with artificial intelligence can be a promising tool for clinical use.

Funding

Disclosures

The authors declare that there are no conflicts of interest related to this article.